An Initial Look at Acceleration-Modulated Thermal Convection

Jeffrey L. Rogers, Michael F. Schatz, Werner Pesch, and Oliver Brausch

1 Introduction

The formation of patterns in spatially extended nonequilibrium systems is a problem of fundamental interest in a broad set of disciplines including physics, engineering, chemistry, and biology. Two of the most commonly studied systems are drawn from hydrodynamics: a fluid layer with an imposed vertical temperature difference (Rayleigh-Bénard convection [1–3]) and an open dish of vertically oscillated fluid (Faraday surface waves [4]). These systems do share common features. For sufficiently weak driving (thermal and vertical vibrations, respectively) both systems are in macroscopically time-independent and uniform states. As driving is increased regular spatial variations appear at well-defined thresholds and the dynamics become complex in space and time when the driving is sufficiently large. However, Rayleigh-Bénard convection and Faraday waves each represent different classes of spatially extended systems, since basic mechanisms of pattern formation differ between these two cases in important ways.

One important distinction is the mechanism which selects a pattern's length scale. At the onset of fluid motion in Rayleigh-Bénard convection, the pattern will display a wavenumber dependent on the geometrical constraints. In particular, the pattern wavenumber q is directly proportional to the fluid layer depth (Fig. 1). Patterns of the geometry-induced type occur in a number of other systems, for example in the buckling of thin plates [5]. In contrast, Faraday surface waves are driven by vertical vibration, often sinusoidal with a drive period τ. This time-dependent driving leads to wavenumber selection by the forcing frequency via a dispersion relation. Other examples of such dispersion-induced [6] patterns include optical waves in a fiber laser [7] and crystallization waves in ^{4}He [8].

Another important distinction between Rayleigh-Bénard convection and Faraday surface waves is the way system symmetries arise and dictate the pattern planform near onset. Patterns in both systems may exhibit inversion symmetry; the equations governing the pattern mode amplitudes A are invariant under the operation $A \to -A$. This symmetry excludes even order terms in the amplitude equations, thereby, strongly influencing the pattern structure near onset. In Rayleigh-Bénard convection, inversion symmetry takes

the form of the Boussinesq symmetry; spatial invariance under vertical reflection about the fluid layer mid plane and is manifested by the stationary stripe patterns typically observed at convective onset. By contrast, inversion symmetry in Faraday waves is temporal, viz., invariance under discrete time translation by τ and is displayed in the subharmonic (periodic at 2τ) waves frequently observed near onset.

Inversion symmetry can be broken in distinct ways in these systems, leading to differences in pattern forming behavior. Breaking inversion symmetry permits quadratic terms in the amplitude equations, leading to pattern selection dominated by three-mode interactions (*resonant triads*) [9]. In convection experiments, the Boussinesq symmetry is typically broken by the spatial dependence of fluid properties in the layer [1,10]. This effect becomes significant when the imposed temperature difference is sufficiently large. The corresponding resonant triad interactions typically lead to the appearance of hexagonal patterns at onset [10,11]. For Faraday waves, inversion symmetry may be broken in a number of different ways [12–14] involving careful choice of the time-dependence of the drive. The character of the resulting resonant triads can depend sensitively on the choice of drive frequencies and therefore, unlike standard Rayleigh-Bénard convection, pattern selection with broken symmetry can be flexibly tuned for Faraday waves.

Recently, pattern formation studies have extended the focus to include the emergence of what Pismen [15] has termed complex-ordered states. These spatially complex patterns are described by a finite number of peaks in the spectral domain and may be classified as quasicrystals or superlattices using the criteria defined by Lifshitz [16]. Essentially, if the number of vectors (indexing vectors) required to span the stimulated modes is greater than the pattern dimension the state is a quasicrystal [16]. Accordingly, if the number of vectors equals the pattern spatial dimension, the state is periodic. Hence, a superlattice is a pattern whose power spectrum contains a finite number of modes which are indexed by a number of vectors equal to the spatial dimension of the pattern. Quasicrystals and superlattices have been reported in other hydrodynamic [12,13,17–19] and optical systems [20,21]. Features generally found among the examples where complex-order has previously been observed include a nearby codimension-two point and multiple accessible wavenumbers.

Many of the characteristics that are distinctive to either Rayleigh-Bénard-type or Faraday-type patterns can be found in a single system: a fluid layer driven by both heating from below and sinusoidal vertical oscillations (Fig. 1). A classical Rayleigh-Bénard convection experiment (no vertical oscillations) of infinite lateral extent is described by two nondimensional parameters: Rayleigh number R and Prandtl number Pr. These parameters are defined,

$$R = \frac{\alpha g d^3 \Delta T}{\nu \kappa} \qquad \text{and} \qquad Pr = \frac{\nu}{\kappa}, \tag{1}$$

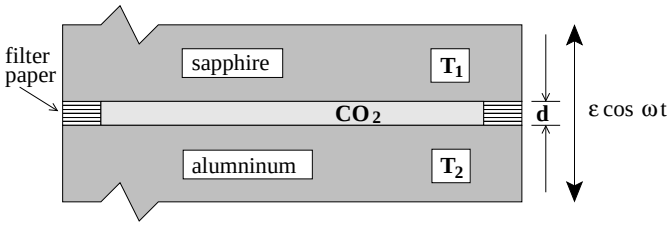

Fig. 1. Sketch of convection cell (not to scale). The relatively thin CO_2 layer of depth d is driven away from equilibrium by an imposed temperature difference ΔT and vertical oscillations ($\varepsilon \cos \omega t$). The top and bottom surfaces are maintained at uniform temperatures T_1 and T_2, respectively ($\Delta T = T_2 - T_1$). Oscillations are defined in terms of the dimensionless acceleration ε and ω (2).

in terms of ΔT (Fig. 1), gravitational acceleration g, d (Fig. 1), thermal diffusivity κ, kinematic viscosity ν, and thermal expansivity α. Intrinsic scales in the experiment are d and the vertical diffusion time ($t_v = \kappa/d^2$). Imposing vertical oscillations on Rayleigh-Bénard convection [22,23] (acceleration-modulated Rayleigh-Bénard convection) results in two additional nondimensional parameters that are analogous to those used to characterize states in Faraday wave experiments: the displacement amplitude δFr and the modulation frequency ω;

$$\delta Fr = \frac{\kappa^2}{d^4 g}\delta' \qquad \text{and} \qquad \omega = \frac{d^2}{\kappa}\omega', \tag{2}$$

where δ' is the dimensional displacement amplitude and ω' is the dimensional angular frequency of oscillation. It is important to note that unlike the Faraday waves there is no free surface in the present case.

In this paper we report the first experimental results for acceleration-modulated Rayleigh-Bénard convection [24–26], which we confirm and augment with a number of new numerical findings [27]. Brief descriptions of our experimental apparatus and numerical methods are presented in Sects. 2.1 & 2.2, respectively. Most of the presented results are for a fixed $Pr = 0.930$ and $\omega \approx 100$. Predicted modulation induced shifts in onset R (R_c) and onset q (q_c) are compared in Sect. 3.1 with experimental observations. In Sect. 3.2 patterns are confirmed to display harmonic (synchronous to the oscillations) and subharmonic temporal dependence for the appropriate parameter values. Harmonic patterns near onset and away from onset are reported and discussed in Sects. 3.3 & 3.4. Examples of subharmonic patterns near and away from onset are presented in Sects. 3.5 & 3.6. For sufficiently large R a direct transition between purely harmonic and purely subharmonic patterns is found to occur. Boundaries for this gradual transition and typical coexisting patterns are investigated in Sects. 4.1 & 4.2. Over a wide range of parameters novel complex-ordered patterns are reported. These complex states are found to be

superlattices, one type of which is found to emerge directly from conduction at a point of codimension-two. The presence of inversion symmetry is found to be important to the coexistence pattern observed near onset. We propose a resonance mechanism for the formation of observed superlattices in Sect. 5.3. Complex-ordered patterns at other ω values are investigated numerically and experimentally in Sect. 5.4.

2 Laboratory

2.1 Experimental Apparatus

Performing the experiments requires vertically oscillating a convection cell (Fig. 1), while controlling the relevant physical quantities to vary the dimensionless parameters in the appropriate manner. The experiment is composed of a convection cell, means for controlling cell temperatures and pressure, a mechanical shaking device, an image acquisition system, and computers to analyze the various data streams. In this section we briefly describe each of these sub-systems. For a more detailed description see [26].

The convection apparatus is based on well-tested designs for standard Rayleigh-Bénard convection using compressed gases [28,29]. The actual convection cell is bounded from below by a 5.08 cm-diameter, 0.60 cm-thick aluminum mirror; from the side by a 3.8 cm-inner-diameter, 5.08 cm-outer-diameter stack of filter paper; and from above by a 5.0 cm-diameter, 2.54 cm-thick sapphire crystal. The cell is confined in an aluminum pressure containment vessel. The sapphire crystal is held tightly against the top of the vessel by the pressure of the compressed CO_2 gas. The aluminum mirror is aligned parallel to the bottom of the sapphire crystal by a kinematic mount with an additional pull-down screw. Interferometry measurements demonstrate that the bounding surfaces remain level when oscillations are imposed.

Fluid properties are under dynamic computer control. Temperature control is provided by heating through a resistive pad the bottom mirror while cooling with a water bath the sapphire crystal. The heating and the cooling are both under computer control allowing the fluid layer mid-plane temperature $\overline{T}$ and ΔT to be held fixed within $\pm 0.01^\circ$ C. The containment vessel is filled with 99.99% pure CO_2, typically at a pressure near 32.72 bar. Pressure is computer-controlled through the heating of a ballast allowing constant pressure to be maintained to $\pm$ 0.01 bar

Vertical oscillations are supplied by hydraulically-driven mechanical shaking systems. The convection apparatus is attached to a piston whose motion is driven by the flow of oil at 120 bar. The oil flow is regulated by high-performance electrodynamic servo valves, which, in turn, are driven by a high-current amplifier under closed-loop control. Thus, controlled oscillations of the piston are achieved by feeding an oscillatory control voltage signal into the amplifier. The displacement amplitude of the oscillations is measured by two devices: a linear variable displacement transducer (LVDT) attached

directly to the piston and an accelerometer attached to the bottom of the containment vessel. The hydraulic shaker is rigidly attached to a heavy mount (ballast), which in turn, rests on elastic supports to damp out vibrational recoil. Lateral vibrations are held to approximately 0.2 % of the vertical motion through the use of a rectangular air-bearing assembly on the drive shaft.

Patterns are visualized using the established method of shadowgraphy [28,29]. Utilizing compressed gases greatly enhances the sensitivity of the shadowgraph [28], since the refractive index is reinforced and the contrast is enhanced by the very thin layers ($d = 0.0650$ cm) which may be used. Shadowgraph images are captured using a ccd camera interfaced with a computer-controlled frame grabber. The image acquisition is synchronized with the shaker drive by use of a ferroelectric liquid crystal shutter. Pattern images are acquired at a predefined phase of the oscillation.

Recorded images are analyzed predominantly in terms of average spectral quantities. To each image a radial Hanning function is applied to reduce aliasing, prior to performing a spatial Fourier transform. The constituent phase angles and power spectra $[\wp(q)]$ is found for each pattern. Generally, the power spectrum are normalized by the windowed image variances so that the total power in the spectrum will sum to unity. The power spectrum are then azimuthally averaged to produce the radial spectrum. Radial power spectrum for all the images at a data point are then averaged. The resulting distribution in q is described by the first two moments,

$$< q > = \frac{\int_{q=0}^{\infty} q^2 \wp(q) dq}{\int_{q=0}^{\infty} q \wp(q) dq} \tag{3}$$

$$< q^2 > = \frac{\int_{q=0}^{\infty} q^3 \wp(q) dq}{\int_{q=0}^{\infty} q \wp(q) dq} \tag{4}$$

Patterns at a given set of parameters may then be characterized by three spectral quantities: the relative power, characteristic q ($< q >$), and the width of q ($\sigma = \sqrt{< q^2 > - < q >^2}$). Some patterns may contain multiple distinct wavenumbers. In these cases, 8^{th}-order Butterworth filters are applied to remove frequency components outside the band being considered.

2.2 Numerical Methods

The convective flow can be described by the Oberbeck-Boussinesq equations, which, when nondimensionalized by d and t_v, take the form

$$\begin{aligned} \nabla \cdot \boldsymbol{v} &= 0 \\ \nabla^2 \boldsymbol{v} + \hat{\boldsymbol{z}}(1 + \frac{\delta' \omega'}{g} \cos \omega t)\Theta - \nabla P &= \frac{1}{Pr}(\boldsymbol{v} \cdot \nabla \boldsymbol{v} + \frac{\partial \boldsymbol{v}}{\partial t}) \\ \nabla^2 \Theta + R\hat{\boldsymbol{z}} \cdot \boldsymbol{v} &= \boldsymbol{v} \cdot \nabla \Theta + \frac{\partial \Theta}{\partial t}, \end{aligned} \tag{5}$$

where $\boldsymbol{v}$ is the velocity, Θ the convection modification of the linear heat conduction temperature profile, and P the pressure. In the co-moving frame to the layer, the effect of modulation appears only in the time-dependent buoyancy term $\hat{\boldsymbol{z}}(\frac{\delta'\omega'}{g}\cos\omega t)\Theta$ [22,23]. The Boussinesq symmetry is not broken by the modulation.

Numerical simulations of (5) are performed by modifying well-tested numerical techniques for standard Rayleigh-Bénard convection. Only minor modifications are required since the time-dependent buoyancy (a linear term) is integrated explicitly in time by employing the approach used previously for quadratic nonlinearities [30]. The equations are solved using isothermal ($\Theta = 0$), no-slip ($\boldsymbol{v} = 0$), and no penetration ($\partial_z \boldsymbol{v}_z = 0$) boundary conditions at the confining (upper and lower) plates. The boundary conditions are enforced by expanding all fields in appropriate test functions (trigonometric or Chandrasekhar functions) [23]. The incompressibility condition $\nabla \cdot \boldsymbol{v} = 0$ is satisfied by the introduction of a poloidal and a torroidal velocity potential. We follow closely the standard approach [23] by expanding all fields into a Fourier series in time combined with a Galerkin expansion in the $z-$direction. Linearization permits calculation of both R_c and q_c as function of the modulation parameters, δFr and ω (Fig. 2). Nonlinear stripe solutions are calculated within the Galerkin approach and examined for secondary bifurcations.

In some cases we include non-Boussinesq effects using the same approach employed for non-Boussinesq effects in standard Rayleigh-Bénard convection [1]. In brief, the temperature dependence of all material parameters is expanded about $\overline{T} = \frac{1}{2}(T_1 + T_2)$ to linear order. This results in both non-Boussinesq corrections obtained for standard Rayleigh-Bénard convection [1] and modification of the time-dependent buoyancy term via the temperature dependence (at quadratic order) of the density. For a more detailed description of the numerical methods see [27]

3 Onset, Time-Dependence, and Typical Patterns

The conduction state competes with temporally modulated convection over a wide range of parameter values. Our studies focus on this competition for the case of fixed Pr and ω. By varying the remaining control parameters δFr and R over a range where R is not too large, the conduction state is found to lose stability to flows with either a harmonic or subharmonic temporal response. Linear stability analyses [22,23] of the current experiment indicate that each type of temporal flow occurs at a distinct spatial scale (Fig. 2). Harmonic flows are predicted to be more stable than unmodulated convection, *i.e.*, the R_c for harmonic convection R_c^H is found to be larger than the R_c in the absence of modulation ($R_c^0 = 1708$). In contrast, subharmonic flows may be either more stable ($R_c^S > R_c^0$) or less stable ($R_c^S < R_c^0$). The q_c of subharmonic patterns q_c^S is typically significantly larger than q_c of harmonic patterns q_c^H [Fig. 2(b)].

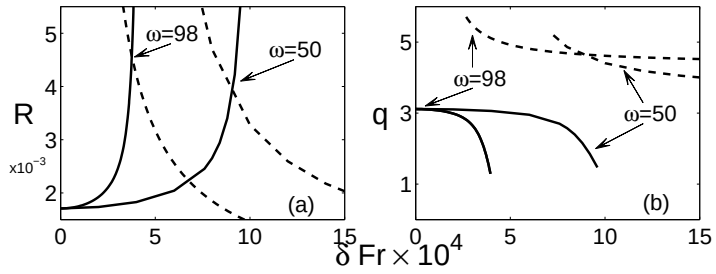

Fig. 2. Linear stability of acceleration-modulated Rayleigh-Bénard convection. Solid lines are marginal stability curves for harmonic response, while dashed lines indicate subharmonic marginal stability curves. Arrows in (**a**) point to bicritical points at the labeled values of ω (= 98 & 50).

3.1 Onset Measurements

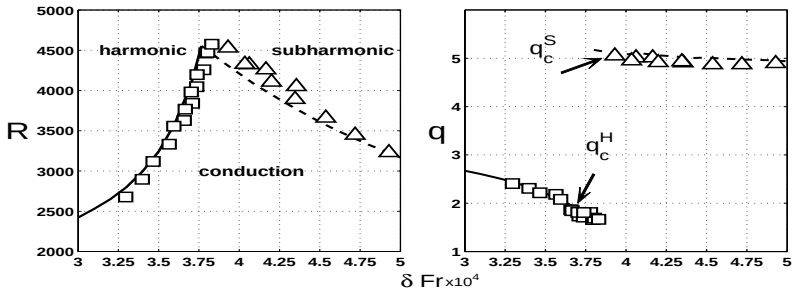

Fig. 3. Comparison of conduction marginal stability predictions to experimental observations of R_c (**a**) as well as q_c (**b**) at $Pr = 0.930$ and $\omega = 98.0$. Solid lines are predicted values for onset of harmonic convection and dashed lines for subharmonic convection. Experimental observations for harmonic and subharmonic ($\triangle$) flows are in quantitative agreement with predictions.

Linear stability predictions of the onset of fluid motion due to parametric modulations are quantitatively confirmed by laboratory observations. In the absence of modulations ($\delta Fr = 0$, $\omega = 0$) the experiment reduces to classical Rayleigh-Bénard convection where it is known conduction loses stability at R_c^0 with $q_c^0 = 3.117$. For these parameters, we observe parallel stripes at onset, suggesting that non-Boussinesq effects are weak and not observable within the resolution of our measurements. Figure 3(a) compares conduction marginal stability boundaries to experimental measurements of the boundary between conduction and convection. With increasing δFr conduction is increasingly stabilized until the harmonic marginal stability curve inter-

sects the subharmonic marginal curve. At the point of intersection (*bicritical point*) conduction loses stability to two different spatial scales simultaneously as R is increased. For $\omega = 98.0$, our linear stability predicts bicriticality at $\delta Fr_{2c} = 3.768 \times 10^{-4}$ & $R_{2c} = 4553$. For $\delta Fr > \delta Fr_{2c}$, the stability analyses and experiments find the slope of the marginal stability curve changes sign. For sufficiently large δFr, beyond the accessibility of the current experiments, onset is predicted to occur for $R < R_c^0$ [23] [see also Fig. 2(a)]. The stability predictions of q_c^H and q_c^S are compared with experimentally measured values in Fig. 3(b). For $\delta Fr < 3 \times 10^{-4}$, the onset wavenumber changes only slightly from q_c^0. With increasing δFr, q_c^H begins to decrease. With $\delta Fr \geq \delta Fr_{2c}$, subharmonic convection arises with a substantially larger q than harmonic convection. Both experiments and the stability analyses find q_c^S remains relatively constant for the range of $\delta Fr \geq \delta Fr_{2c}$ studied. Neither harmonic nor subharmonic onset exhibited hysteresis within the resolution of our experiments.

3.2 Confirmation of time-dependence

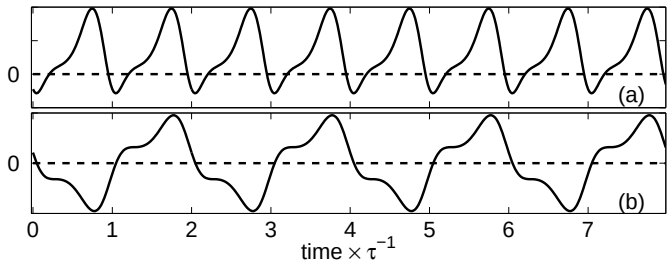

Fig. 4. Temporal dependence of Fourier modes (*simulation*) in the fluid horizontal mid plane of (**a**) purely harmonic convection and (**b**) purely subharmonic convection.

To investigate the fluid's temporal dependence multiple images are recorded during a single τ, each separated by a constant time interval. Temperature time series from the simulations indicate that harmonic convection oscillates about nonzero mean [Fig. 4(a)] with a period of τ; shadowgraph images [Fig. 5(a) & 5(b)] from the experiments demonstrate flows with period τ. By contrast, simulations indicate the subharmonic temperature field oscillates about zero mean with a period of 2τ [Fig. 4(b)]. Oscillations in the subharmonic temperature field must satisfy the subharmonic time-translation (inversion) symmetry which requires the field variables invert under discrete time translation by τ. This effect of symmetry is observed in the experiments as time-periodic switching of the temperature field. Shadowgraph images separated

in time by an odd multiple of τ demonstrates switching between the upflow (light) and downflow (dark) regions of the pattern [Fig. 5(c) & 5(d)].

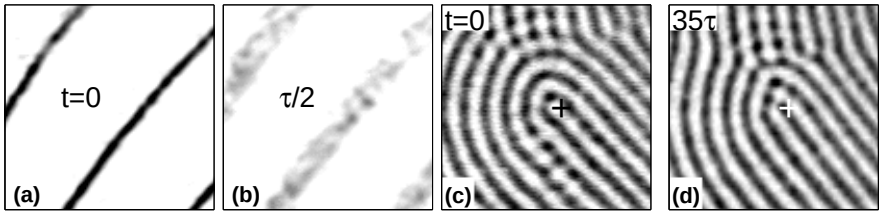

Fig. 5. Shadowgraph (*experiment*) of singly resonant flows. Purely harmonic patterns (**a** & **b**) repeat every τ time interval. At $t = 0$ (**a**) the stripe state is well-defined. For odd multiples of τ (**b**) the stripe state becomes broader, while at even multiples of τ the original state (**a**) repeats. Each 128 by 128 pixel frame is over the same spatial location separated in time by $\tau/2$. In contrast, purely subharmonic patterns (**c** & **d**) invert every τ time-interval. Note, the + signs near the image (**c** & **d**) centers, these are plotted at the same coordinates in both frames. The disclinations center stripe is light at even multiples of τ [(**c**) t=0] and dark at odd multiples of τ [(**d**) $t = 35\tau$].

3.3 Harmonic Patterns at Onset

Harmonic patterns at onset are striped and may contain domains of hexagons depending on R. Parallel stripes [Fig. 6(a)] and targets [Fig. 6(b)] are typically observed at onset. These patterns may be found anywhere ($2000 < R < 4500$) along the harmonic stability curve (Fig. 7), while domains of hexagons only occur close to onset at larger R values ($3800 < R < 4800$). From classical Rayleigh-Bénard convection studies in compressed gases ($Pr \approx 1$) it is known that parallel stripes form when the side wall forcing is minimal and that cell filling (giant) targets or spirals [31] are present near onset when the side wall forcing is more significant (for example, due to side wall heating [32]). We expect a similar mechanism to be at work in our experiments where the selection of stripes or targets varies with different experimental configurations. Thus, we associate stronger side wall forcing from the circular lateral boundary with the onset of targets and weaker side wall forcing with parallel stripe formation. Targets may display light or dark cores, designating cold (downflowing) or warm (upflowing) centers, respectively. Domains of hexagons may be present in both striped and target base states at larger R values with the domains of hexagons becoming larger with R [Figs. 6(c) & 6(d)]. Hexagons with both downflowing centers [Fig. 6(c) & 6(d)] and upflowing centers are observed. Transitions between domains of locally upflowing and downflowing hexagons are also observed. The presence of hexagonal domains indicates the approximation of Boussinesq symmetry is not valid near

onset for at relatively large R. Similar mixed stripe-cellular patterns have been observed previously in temperature-modulated Rayleigh-Bénard convection experiments [33]. Physically this is likely due to the temperature dependence of fluid properties; the variation of these properties within the layer increases with increasing R (increasing ΔT) and explains why hexagons are most readily observed when the onset of harmonic convection occurs at the largest values of R near R_{2c}. Over most of the purely harmonic region the majority of stable states are strikingly similar to patterns found in classical Rayleigh-Bénard convection studies (without modulation) [32].

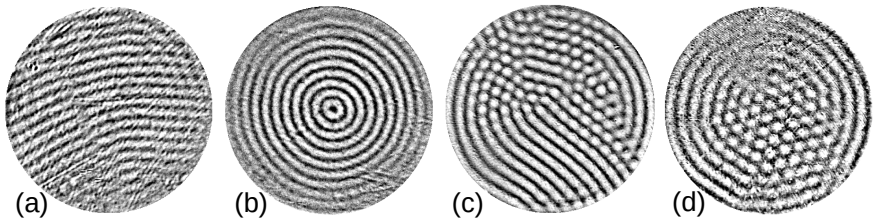

Fig. 6. Harmonic onset striped patterns include: (**a**) parallel stripes ($\delta Fr = 3.34 \times 10^{-4}$, $\omega = 97.8$, & $R = 3002$), (**b**) targets ($\delta Fr = 3.29 \times 10^{-4}$, $\omega = 98.0$, & $R = 2979$), (**c**) stripes with hexagons ($\delta Fr = 3.71 \times 10^{-4}$, $\omega = 96.2$, & $R = 4388$), and (**d**) targets with hexagons ($\delta Fr = 3.76 \times 10^{-4}$, $\omega = 96.6$, & $R = 4107$).

3.4 Harmonic Patterns Away from Onset

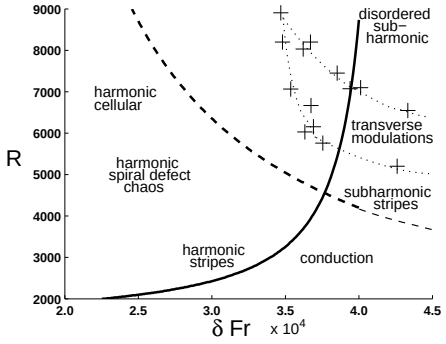

Fig. 7. Parameter space showing conduction marginal stability curves for harmonic (*solid*) and subharmonic (*dashed*) convection as well as experimental determined regions of behavior.

Onset patterns undergo a transition to spiral defect chaos as the system moves from conduction further into the convection regime by combinations of decreasing δFr and increasing R (Fig. 7). Two different scenarios are observed, depending upon whether the transition sequence begins with either parallel stripes or target patterns. The domains of hexagons observed near onset at larger R play no role in this transition sequence because, for small decreases in δFr away from onset, hexagons disappear and only patterns of either stripes or targets remain.

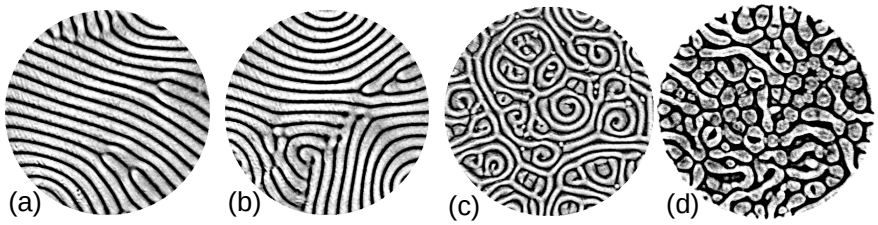

Fig. 8. Examples of typical patterns observed moving away from onset stripes: (**a**) stripes with point defects and two wall foci forming ($\delta Fr = 3.47 \times 10^{-4}$, $\omega = 98.4$, & $R = 3926$), (**b**) three-foci stripes ($\delta Fr = 3.36 \times 10^{-4}$, $\omega = 98.4$, & $R = 3926$), (**c**) spiral defect chaos ($\delta Fr = 2.06 \times 10^{-4}$, $\omega = 96.2$, & $R = 4385$), and (**d**) harmonic cellular ($\delta Fr = 2.70 \times 10^{-4}$, $\omega = 100.3$, & $R = 8077$).

The transition from parallel stripes to spiral defect chaos is similar to that observed in classical Rayleigh-Bénard convection [32]. Moving away from onset, stripe curvature increases, forming focus singularities at the lateral boundaries, as the stripes increasingly align themselves perpendicular to the side walls. Initially, two foci will form [Fig. 8(a)] with the stripe curvature increasing as the experiment is tuned away from onset. Two-foci patterns are similar to the so-called Pan-Am states observed in classical Rayleigh-Bénard convection at comparable Pr and aspect ratio [34,35]. Away from onset, stripe curvature gradually increases and more wall foci form [Fig. 8(b)] leading to local frustration of the pattern wavenumber and formation of point defects. These defects typically include locations where two stripes are replaced by a single stripe (dislocations) and lines of point defects where the pattern amplitude goes to zero (amplitude grain boundaries). Dislocations increase in number as the experiment moves away from onset, while amplitude grain boundaries are typical in stripe patterns with 3-foci. Generally, once the number of wall foci is larger than four, spirals will begin to appear in the interior of the pattern. The system then begins to display states composed of left and right handed spirals [Fig. 8(c)]. As spiral defect chaos gradually fills the convection cell, the harmonic wavenumber q^H remains well-defined, but the corresponding peak width σ^H increases. The emergence of dislocations and grain boundaries, focus singularities, and the broadening of q distribution

about a characteristic value observed in the transition from stripes to spiral defect chaos is also seen without modulation [32]. With both sufficiently large δFr and relatively large R, q^H becomes less well-defined and σ^H becomes large as spiral defect chaos gradually gives way to cellular patterns without spirals [Fig. 8(d)].

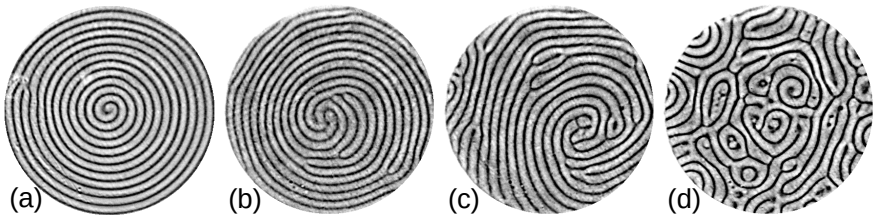

Fig. 9. Moving into the convection regime from a onset target typically observed patterns include: (**a**) one arm spirals ($\delta Fr = 1.74 \times 10^{-4}$, $\omega = 98.4$, & $R = 2479$), (**b**) multi arm spirals with defects ($\delta Fr = 1.95 \times 10^{-4}$, $\omega = 99.4$, & $R = 2422$), (**c**) off-center multi arm spirals with defects ($\delta Fr = 2.26 \times 10^{-4}$, $\omega = 99.0$, & $R = 2936$), and (**d**) spiral defect chaos ($\delta Fr = 2.30 \times 10^{-4}$, $\omega = 98.5$, & $R = 3663$.)

When the side wall influence is more substantial the onset striped pattern is a target and the transition to spiral defect chaos is somewhat different. Moving away from onset a defect mediated transition from targets to spirals occurs. Pairs of defects emerge in the pattern due to skew-varicose instabilities. One defect from each pair will translate radially to the spiral core producing a one arm spiral while the other defect will translate radially to the side walls and annihilate. In Fig. 9(a) the defect pair originated in a target near the core producing the one arm spiral, the other defect is translating to the side walls. Sufficiently near onset continual nucleation can result in switching between targets and one arm spirals [26]. Continuing away from onset additional defects enter the pattern due to skew-varicose instabilities producing multi arm spirals, as many as six arm spirals are observed. Occasionally, an additional instability results in the targets or spirals cores moving off-center. An example of this instability in shown in Figs. 9(b) & 9(c) for a three arm spiral. Further away from onset, skew-varicose and off-center instabilities result in numerous defects throughout the pattern and the giant spiral will become unstable as spiral defect chaos [Fig. 9(d)] forms [31]. Moving to larger R at sufficient δFr spiral defect chaos gradually gives way to patterns like Fig. 8(d). The transition from spiral defect chaos to states like Fig. 8(d) is qualitatively independent of the onset planform.

3.5 Subharmonic Patterns at Onset

At onset, observed subharmonic states are parallel stripes [Fig. 10(a)] that may include defects [Fig. 10(b-d)]. In contrast to the harmonic flows, hexagons

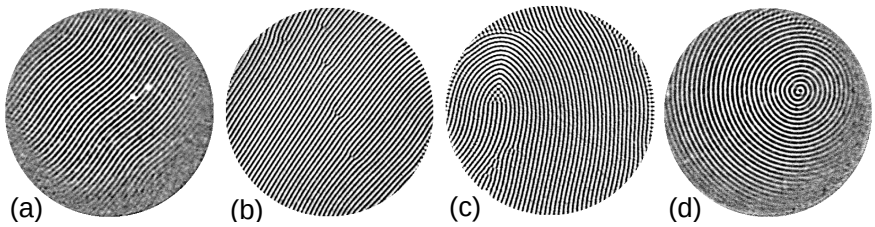

Fig. 10. Examples of patterns observed near onset of subharmonic convection. Patch (**a**) of parallel stripes ($\delta Fr = 4.02 \times 10^{-4}$, $\omega = 97.9$, & $R = 4395$), (**b**) parallel stripes with dislocations ($\delta Fr = 3.74 \times 10^{-4}$, $\omega = 97.9$, & $R = 4857$), (**c**) stripes with a giant convex disclination and several dislocations ($\delta Fr = 3.34 \times 10^{-4}$, $\omega = 97.5$, & $R = 4811$), and (**d**) onset spiral ($\delta Fr = 4.12 \times 10^{-4}$, $\omega = 97.9$, & $R = 4173$).

are not observed anywhere along the subharmonic marginal stability curve. This is expected, due to the temporal subharmonic inversion symmetry, which excludes the resonant triads.

Giant convex disclinations are common near onset, while cell filling concave disclinations are not observed. Cell filling subharmonic spirals [Fig. 10(d)] can arise when side wall forcing is sufficiently large. However, subharmonic spirals are unusual even when sidewall forcing is sufficient to induce targets or spirals at the onset of harmonic convection. Only one and three arm giant spirals have been observed. If giant convex disclinations [Fig. 10(c)] or giant spirals form at onset they are typically centered about the midpoint of the convection cell and move off center as the system begins to move away from onset. Sufficiently far from onset, the cores of convex disclinations annihilate at the lateral boundary leaving a parallel stripe pattern. Due to the characteristic wave length of subharmonic patterns being substantially smaller than that of harmonic patterns it might be expected that side wall forcing would have less of an influence over the selected planform.

3.6 Subharmonic Patterns Away from Onset

With combinations of increasing δFr and increasing R (Fig. 7), subharmonic patterns exhibit a transition to disorder that is qualitatively different from that observed for harmonic patterns. In particular, spiral defect chaos is not observed for subharmonic convection. Parallel stripes near onset display cross-roll defects and dislocations as mechanisms to adjust local variations in the pattern wavenumber; q^S slowly decreases away from onset. Further from onset, wall foci form as stripes begin to show curvature [Fig. 11(a)]. Two and three foci stripes are common, with three foci patterns often containing a amplitude grain boundary near the pattern center. These states often contain several dislocations and regular spacing of the focal singularities. For δFr and R sufficiently large (Fig. 7), patterns with transverse modulations

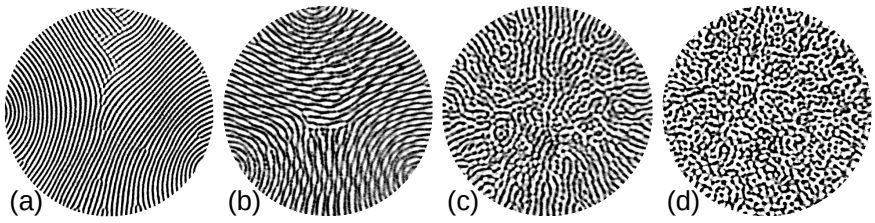

Fig. 11. Examples of typical subharmonic patterns observed away from onset: (**a**) two-foci stripes with defects ($\delta Fr = 4.17 \times 10^{-4}$, $\omega = 98.1$, & $R = 4888$), (**b**) three-foci transverse modulated stripes ($\delta Fr = 4.01 \times 10^{-4}$, $\omega = 98.0$, & $R = 6552$), radial stripes - onset of subharmonic disorder ($\delta Fr = 4.83 \times 10^{-4}$, $\omega = 95.0$, & $R = 6120$), and (**d**) subharmonic disorder ($\delta Fr = 4.60 \times 10^{-4}$, $\omega = 95.0$, & $R = 7670$.)

[Fig. 11(b)] bifurcate from the parallel stripe state. The focal singularities and point defects present in the pattern prior to the bifurcation are preserved after the emergence of transverse modulations. The transverse modulations propagate along the length of the stripes and oscillate in time with a period that is different from either the harmonic or subharmonic period. Spatial power spectra of the transverse modulated pattern demonstrate that the modulation q is only slightly greater than q^H [Fig. 14(e)]; moreover, the width of the subharmonic peaks σ^S increases significant at the bifurcation. With further increases in δFr and R, transverse modulation disappears as the stripes begin to align themselves radially from the center to the lateral boundary [Fig. 11(c)]. During this transition q^S continues to decrease, while the formation of radial stripes corresponds to a reduction in σ^S. Continuing away from onset the radial stripes begin to lose coherent structure, initially in the pattern interior. Sufficiently far from onset this fragmented state occurs throughout the convection cell [Fig. 11(d)] and retains a characteristic q^S with a σ^S larger than that for radial stripes.

4 Direct Harmonic-Subharmonic Transition

At sufficiently large R conduction is not stable for any δFr and a direct transition between harmonic and subharmonic patterns can occur as δFr is varied. Experiments indicate this transition is not abrupt, but occurs gradually over a range of parameter values where harmonic and subharmonic patterns coexist. Roughly speaking, this coexistence region lies between the conduction marginal stability curves extended into the convection regime (Fig. 12).

4.1 Transition from Pure Harmonics to Coexistence

Purely harmonic patterns [Fig. 13(b)] lose stability to coexisting states with localized regions of subharmonic strips [Fig. 13(b)]. Prior to onset, the har-

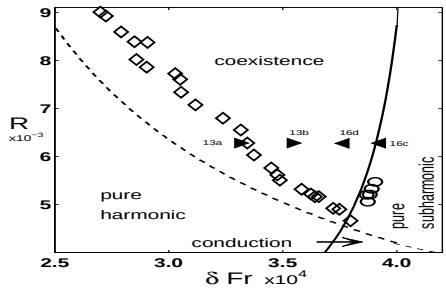

Fig. 12. Phase plane comparing the experimentally measured coexistence onset to the marginal stability curves for conduction. Boundary between coexistent and purely harmonic flows (*diamonds*) follows the marginal subharmonic ($\omega/2$) curve (*dashed*), while the boundary between coexistent and purely subharmonic patterns (*circles*) tracks the marginal harmonic (ω) curve (*solid*) as far as the boundary can be reliably determined. Filled in triangles are the locations of patterns in Figs. 13 & 16.

monic pattern typically consists of parallel stripes with defects. With increasing δFr at constant R, localized domains of subharmonic stripes emerge with a characteristic wavenumber q^S slightly less than $3q^H$. These subharmonic domains are typically either centered about defects in the harmonic pattern or aligned perpendicular to the lateral boundaries [Fig. 13(b)]. Subharmonic stripes at the lateral boundary typically remain pinned to the boundary and do not move into the interior. Harmonic defects continually nucleate, are advected, and annihilate in the pattern interior. These dynamics drive the behavior of the subharmonic patches, which correspondingly appear, move and disappear. Although harmonic defects are virtually always present for parameter values near the pure harmonic-coexistence boundary, not all harmonic defects have associated subharmonics. As a result, near onset, the subharmonic stripe patches are intermittent in time for a range of δFr of width $\sim 4e-06$. Because of intermittency in both space and time, the onset of subharmonics is difficult to detect in spatial power spectra [Figs. 14(a) & 14(b)]. Detection is more reliably performed using the real space images of the patterns. The onset value of δFr for a given R corresponds to the presence of subharmonic patches in the pattern interior for at least 10% of the observation time.

Our results provide evidence that harmonic patterns have an inhibitory effect on the emergence of subharmonic patterns. In the first place, the boundary for convective onset in the experiments lies above the subharmonic marginal stability curve over the entire experimentally accessible range of parameters (Fig. 12). In other words, the subharmonic onset is delayed relative to the linear theory predictions of onset from the conduction state. Furthermore, subharmonics always appear in regions where the harmonic flows are

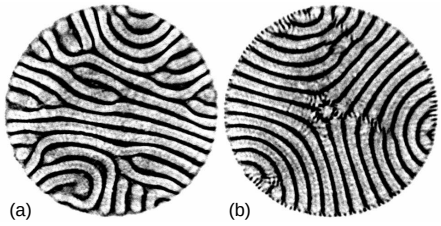

Fig. 13. Patterns on either side of the purely harmonic-coexistence boundary. Pure harmonic stripes (**a**) with defects ($\delta Fr = 3.31 \times 10^{-4}$, $\omega = 98.0$, & $R = 6280$). Coexistence state (**b**) with 3-foci harmonic stripes and subharmonic stripe patches ($\delta Fr = 3.54 \times 10^{-4}$, $\omega = 98.0$, & $R = 6280$).

weaker, namely in the cores of defects amplitude of convection flow is reduced [36].

The subharmonic component remains localized and spatially intermittent even as δFr is increased (with R fixed) to move the system well away from the pure harmonic-coexistence boundary. The subharmonic component is spectrally indistinguishable from the background noise and the second harmonic of q^H over a wide range of δFr [Figs. 15(a), 14(a) & 14(b)]. The wavenumber of the harmonic modes q^H remains relatively fixed [Fig. 15(b)]. The spectral width σ^H decreases [Fig. 15(c)] because the harmonic pattern exhibits fewer defects as the system moves further away from the pure harmonic-coexistence boundary (Fig. 13). The subharmonic pattern component gradually increases with δFr.

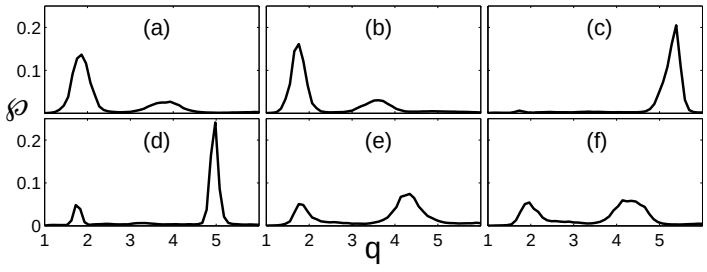

Fig. 14. Azimuthally averaged power spectra for six different experimental conditions from the transition from pure harmonic convection to pure subharmonic convection, passing through a region of coexisting harmonic-subharmonic convection. Representative images from each data point are shown in other figures: (**a**) see Fig. 13(a), (**b**) see Fig. 13(b), (**c**) see Fig. 16(a), (**d**) see Fig. 16(b), (**e**) see Fig. 16(c), and (**f**) see Fig. 16(d).

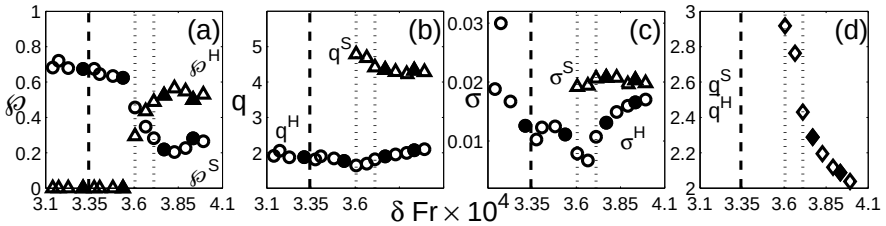

Fig. 15. Average spectral quantities (*experiment*) during a transition from purely harmonic to purely subharmonic patterns by increasing δFr at $R = 6280 \pm 10$. The azimuthally averaged spectra for both the harmonic and subharmonic modes are characterized by (**a**) the power the in harmonic $\wp^H$ and subharmonic $\wp^S$ wavenumber bands, (**b**) q^H & q^S, (**c**) σ^H & σ^S, and (**d**) the wavenumber ratio $\frac{q^H}{q^S}$. Throughout, ○ indicates harmonic pattern component and △ the subharmonic pattern component. Filled in symbols correspond to patterns shown in Figs. 13 & 16. Dotted lines mark the onset of square superlattices (Sect. 5).

4.2 Transition from Pure Subharmonics to Coexistence

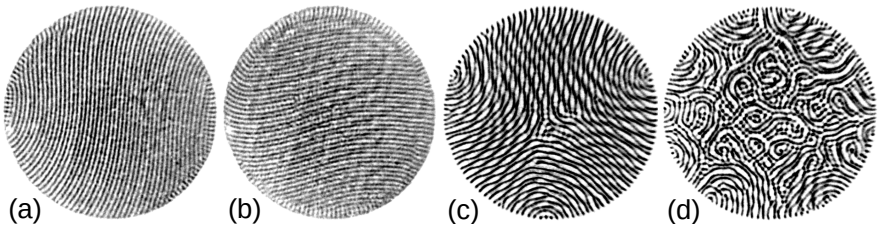

Fig. 16. Patterns on either side of the harmonic-coexistence marginal stability curve ($Pr = 0.930$, $\omega = 98.0$) for $R = 4980$ [$\delta Fr = 3.80 \times 10^{-4}$ (**a**) & $\delta Fr = 3.69 \times 10^{-4}$(**b**)] and $R = 6280$ [$\delta Fr = 3.93 \times 10^{-4}$(**c**) & $\delta Fr = 3.77 \times 10^{-4}$ (**d**)].

The transition from purely subharmonic states to coexisting patterns is qualitatively different from that at onset from pure harmonics. Pure subharmonic patterns lose stability to coexisting states where the harmonic component emerges globally; no localized states are observed. For $\omega = 98.0$, we consider two cases: $R_{2c} < R < 5500$ and $R > 5500$

For $R_{2c} < R < 5500$ the coexistence regime competes with pure subharmonic parallel stripes [Fig. 16(a)]. Slowly decreasing δFr at constant R a harmonic pattern component emerges at a well-defined location in parameter begins to be present throughout the pattern [Fig. 16(b)]. Although the harmonic component is weak at onset, the transition is well-defined and readily detectable in Fourier space by looking for the initial presence of power at q^H [Figs. 14(c) & 14(d)]. Typically, the emerging harmonic component is parallel stripes which may display domains with several orientations. In this

parameter range, this transition is well-predicted by the *conduction* marginal stability curve (Fig. 12), suggesting that the onset of large length scale harmonic convection is neither enhanced or suppressed by the presence of short length scale subharmonic flows. Hysteresis is not experimentally observed in the transition between pure subharmonic flows and the coexistence regime.

For $R > 5500$ the coexistence states compete with more complex pure subharmonic flows. For $5500 < R < 7000$, subharmonics with transverse modulations [Fig. 16(c)] are found when δFr is large (Fig. 7). For $R > 7000$, the subharmonic flows are more disordered [Figs. 11(c) & 11(d)]. As δFr is decreased at constant R to cross the conduction marginal stability boundary, the flow structure changes gradually to patterns like that shown in Fig. 16(d). In all cases, these states are difficult to distinguish spectrally because they contain spectral peaks with similar power content at wavenumbers corresponding to both q^S and q^H [Figs. 14(e) & 14(f)]. As a result, the onset of the coexistence regime from pure subharmonics is ill-defined for this range of R.

Spectral analysis demonstrates that the gradual nature of the transition from pure subharmonics to coexisting patterns continues as δFr is further decreased. For $R < 5500$ the growing harmonic stripes have little effect on the subharmonic stripes as the two components are simply superimposed. For $5500 < R < 7000$ the subharmonic striped base state that supports the transverse modulations gradually breaks down as numerous domains form [Figs. 16(c) & 16(d)]. Typically, these domains nucleate in the pattern interior and spread to fill the pattern with decreasing δFr. For $R > 7000$ the structurally disordered state [Fig. 11(d)] becomes more ordered with decreasing δFr. Regardless of the R value the spectral measures display similar trends. First, relative power in $\wp^S$ gradually decreases and $\wp^H$ slowly increases as the harmonic pattern becomes more significant [Fig. 15(a)]. Eventually, $\wp^S$ contributes $< 60\%$. Second, q^H [Fig. 15(b)] remains relatively fixed while σ^H decreases [Fig. 15(c)]. Simultaneously, q^S slowly increases while σ^S remains relatively constant. These similarities indicate that as the pattern passes further into coexistence the harmonic pattern slowly grows and becomes more regular while $\wp^S$ slowly decrease and q^S increases.

5 Superlattices

Exotic complex-ordered patterns [Fig. 17(a)] abruptly form as the system moves sufficiently far into the coexistence parameter regime. These patterns are reminiscent of recently observed nonequilibrium structures [12–14,17–19] that have been designated as *quasicrystals* (*quasipatterns*) or *superlattices*. The formation of the current complex-ordered structures corresponds to rapid changes in the spectral quantities, including the formation of distinct peaks in the power spectrum [Fig. 17(b)]. Since these twelve peaks can be indexed by only two basis vectors, this pattern is a superlattice [16]. We call patterns

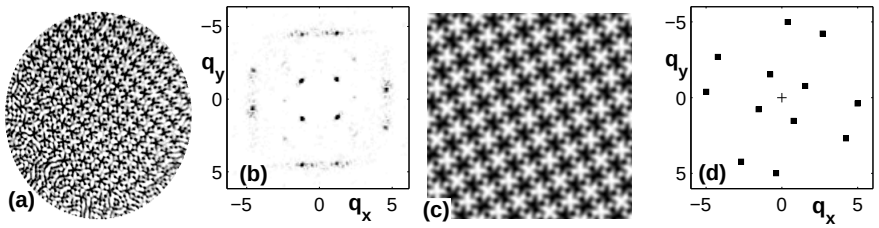

Fig. 17. Square superlattices observed in both experiments (**a**) and simulations (**b**). Parameter values are: (**a**) $\delta Fr = 3.88 \times 10^{-4}$, $\omega = 95.3$, & $R = 7030$ and (**b**) $\delta Fr = 3.75 \times 10^{-4}$, $\omega = 98$, & $R = 4750$.

of this type *square superlattices* [25]. To the best of our knowledge, the patterns observed in this investigation are the first complex-ordered states to be reported in convection experiments. In the related case of heating from above ($R < 0$) a numerical study [37] predicted quasiperiodic structures in the presence of non-Boussinesq effects.

5.1 Observations Near Bicriticality

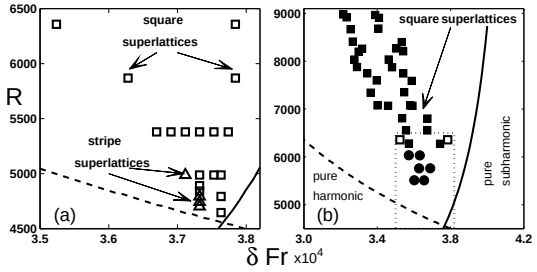

Fig. 18. Phase planes showing the onset of superlattices in (**a**) numerics and (**b**) experiments. *Squares* designate onset of square superlattices, while *triangles* record the observation of stripe superlattices. Open symbols are numerical observations; solid symbols are experimental findings. The parameter range in (**a**) is marked by the dotted box in (**b**).

First, consider observations made in the vicinity of the bicritical point. Numerical simulations of (5) demonstrate that square superlattices [Fig. 17(c)] arise very near the bicritical point (intersection of the solid and dashed lines in Fig. 18). With $\delta Fr = \delta Fr_{2c}$, numerics find square superlattices bifurcate directly from the conduction state at $R = R_{2c}$. Both harmonic and subharmonic modes contain equal spectral power, which increases continuously

from zero as $\sqrt{R - R_{2c}}$, *i.e.,* the square superlattices bifurcate supercritically from conduction. As R increases, the range of δFr where square superlattices are attracting becomes wider [Fig. 18(a)]. These simulations of the inversion symmetric (5) find parallel stripe patterns at both pure harmonic and pure subharmonic onset in the vicinity of the bicritical point.

A second type of complex-ordered state is observed numerically near the bicritical point when $\delta Fr < \delta Fr_{2c}$ [Fig. 18(a)]. Power spectrum for these patterns display six distinct peaks at two different wavenumbers. Since these spectral peaks can be indexed by two basis vectors, $\boldsymbol{b}_1$ & $\boldsymbol{b}_2$ in [Fig. 19(b)], these states are also superlattices that we call *stripe superlattices.* Increasing R at constant δFr stripe superlattices are found to bifurcate supercritically from the base state of parallel harmonic stripes. Stripe superlattices are bistable with square superlattices over a relatively very narrow parameter range [Fig. 18(a)]. During the initial report of these states [25] we referred to them as *roll superlattices.*

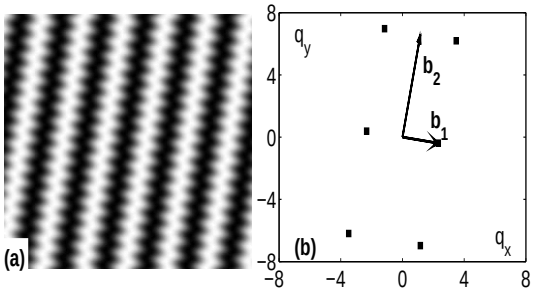

Fig. 19. Numerical solutions of (5) find a periodic complex-ordered pattern over a narrow parameter range [Fig. 18(a)]. These (**a**) stripe superlattices ($\delta Fr = 3.732 \times 10^{-4}$, $\omega = 98$, & $R = 4794$) are constructed of (**b**) spectral modes which can be indexed by two vectors ($\mathbf{b}_1$ & $\mathbf{b}_2$).

Near the bicritical point experiments do not find superlattices. Shown in Fig. 20(a-c) are patterns observed at fixed $\omega = 95.0$ and slowly increasing R. Additionally, δFr values are maintained near the bicritical point ($\delta Fr_{2c} = 3.91 \times 10^{-4}$ & $R_{2c} = 4640 \pm 10$) values. The initial state is conduction. Onset occurs to pure regular harmonic hexagons. Slowly increasing R small localized regions of subharmonic stripes ($R \approx 5100$) occur on the harmonic hexagons [Fig. 20(a)]. Moving further into the coexistence parameter region, harmonic hexagons become less pronounced as domains of locally hexagonal, square and rhombic symmetries begin to form [Fig. 20(b)] [24]. Eventually ($R > 6280$), the harmonic component displays only domains of locally square symmetry as square superlattices emerge [Fig. 20(c)].

The experiment shown in Fig. 20(a-c) suggests non-Boussinesq effects are responsible for superlattices not being experimentally observed near bi-

criticality. The presence of hexagons near the bicritical point suggests non-Boussinesq effects are significant in this parameter region. Physically, the significant variation of fluid properties due to large ΔT ($\approx$ 17°C, in this case) near bicriticality is expected to lead to observable non-Boussinesq effects. Moving further into coexistence, experiments at $\delta Fr \approx \delta Fr_{2c}$ find domains of hexagons coexisting with domains of squares and rhombuses. Numerics that account for temperature-dependent non-Boussinesq effects confirm experimental observations and indicate hexagons form throughout the harmonic component sufficiently near to bicriticality [Fig. 20(d)]. Interestingly, hexagons in coexistence patterns may contain cold and warm centers simultaneously [Fig. 20(d)]. This unexpected hexagon characteristic is also experimentally observed near pure harmonic onset in the vicinity of the bicritical point.

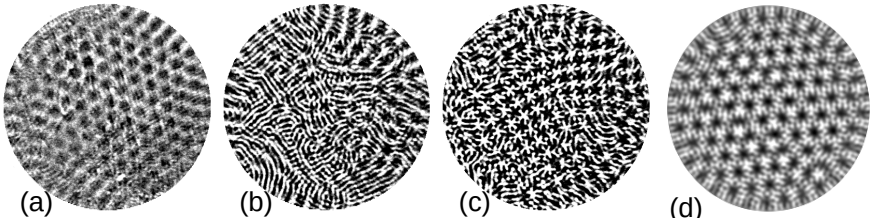

Fig. 20. Coexisting patterns observed in the vicinity of the bicritical point. Experimental patterns (**a-c**) are from a trial passing from conduction by slowly increasing R at δFr slightly less than δFr_{2c}. Simulations including non-Boussinesq effects (**d**) find hexagons in the harmonic component. Corresponding parameters are: (**a**) $\delta Fr = 3.89 \times 10^{-4}$, $\omega = 95.0$, & $R = 4778$, (**b**) $\delta Fr = 3.88 \times 10^{-4}$, $\omega = 95.0$, & $R = 5389$, (**c**) $\delta Fr = 3.73 \times 10^{-4}$, $\omega = 96.7$, & $R = 6267$, and (**d**) $\delta Fr = 3.75 \times 10^{-4}$, $\omega = 98$, & $R = 4750$.

5.2 Observations Away from Bicriticality

Well-ordered superlattices are observed in the experiments for a wide range of parameter values away from the bicritical point. Nearly defect-free square superlattices [Fig. 17(a)] form between $R = 6280$ up to the maximum experimentally accessible $R \sim 9300$ [Fig. 18(b)]. Square superlattices persist over a δFr range where the spectral power in the harmonic and subharmonic modes are approximately equal ($\wp^H \approx \wp^S$ [Fig. 15(a)]). Simulations of (5) at these large values of R well-predict the range of δFr over which square superlattices are observed [Fig. 18(b)]. These results suggests that non-Boussinesq effects are only significant to superlattice formation near the bicritical point.

Experimental results indicate several common features are observed for transitions between superlattices and other coexisting patterns as δFr is varied for fixed R. For small values of δFr in the coexistence regime, the observed

patterns are harmonic stripes with localized patches of subharmonic stripes (Sect. 4.1). With increasing δFr just prior to superlattice onset, harmonic dominated patterns abruptly begin to show significant subharmonic contribution, and the harmonic planform separates into multiple domains. With a small increase in $\delta Fr \sim 5 \times 10^{-6}$, square superlattices abruptly begin to form. At the transition, the harmonic modes contain $\sim$ 60% of the total power and reach minimum values in q^H and σ^H, while q^S is at its maximum value (Fig. 15). Upon further increases of δFr, the superlattice patterns lose stability abruptly to coexistence patterns dominated by subharmonics (Sect. 4.2). At this transition, the subharmonic modes contain ($\sim$ 60%) of the total power and the subharmonic wavenumber q^S decreases with increasing δFr. The harmonic modes increase in q^H with $\wp^H$ remaining finite (Sect. 4.2). The relaxation time for the formation of a single domain of square superlattices becomes substantially larger near the transition boundary with both harmonic-dominated and subharmonic-dominated coexistence patterns. No hysteresis is observed at the transitions from superlattices to other coexistence patterns.

5.3 Resonant Tetrads

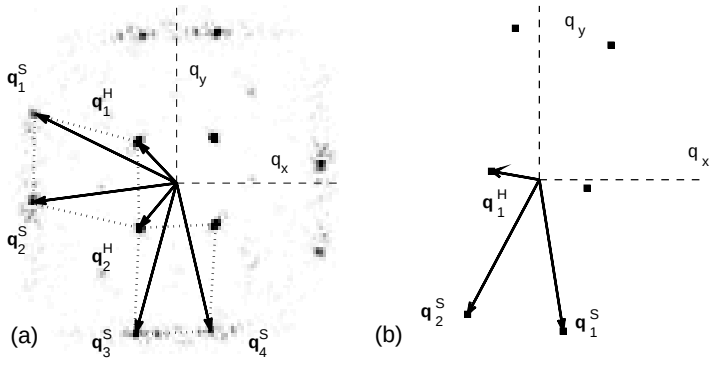

Fig. 21. Power spectra for (**a**) the square superlattice (*experiment*) in Fig. 17(**a**) and (**b**) the stripe superlattice (*simulation*) shown in Fig. 19(**a**).

Power spectra for the superlattice patterns demonstrate that the complex spatial structure of these states are described by a few spectral modes. Square superlattices (Fig. 17) have spectra with twelve dominant peaks at two distinct wavenumber bands [Fig. 21(a)]. The four peaks $\pm(\mathbf{q}_1^H, \mathbf{q}_2^H)$ correspond to the square sublattice, which displays a harmonic temporal response. The eight peaks at the larger $[\pm(\mathbf{q}_1^S, \mathbf{q}_2^S, \mathbf{q}_3^S, \mathbf{q}_4^S)]$ correspond to the small length scale "star" sublattice, which displays a subharmonic temporal response. Stripe superlattices exhibit six dominant peaks. The harmonic

stripe sublattice corresponds to the two peaks at $\pm\mathbf{q}_1^H$ while subharmonic sublattice corresponds to peaks at $\pm(\mathbf{q}_1^S, \mathbf{q}_2^S)$.

Interactions between the modes from the harmonic and subharmonic sublattices are found to satisfy resonance conditions. Spectral changes made as the experiment passes into the square superlattice parameter regime are suggestive of interactions between the harmonic and subharmonic sublattices. During the transition to square superlattices the power, which is typically distributed in azimuthally averaged wavenumber bands q^H & q^S, moves to a few discrete spectral peaks on the two sublattices. These peaks will form the vertices of parallelograms between two of the harmonic and a pair of the subharmonic peaks [Fig. 21(a)]. Existence of these parallelograms suggests the four wave resonance (*resonant tetrad*) conditions:

$$\pm(\mathbf{q}_1^H - \mathbf{q}_2^H) = \pm(\mathbf{q}_1^S - \mathbf{q}_2^S) \quad \text{and}$$
$$\pm(\mathbf{q}_1^H + \mathbf{q}_2^H) = \pm(\mathbf{q}_3^S - \mathbf{q}_4^S). \tag{6}$$

Square superlattices in both experiments and numerics always satisfy these resonant tetrad (6) conditions. In the vicinity of the bicritical point, numerics find the mode parallelograms become rectangles. Further from onset, translations of the subharmonic peaks along the straight lines allows the $|\mathbf{q}_i^S|$ ($i = 1...4$) to take on different values for all i, while always satisfying (6). Experiments indicate that with increasing R square superlattices are composed of relatively constant q^H ($0.91q_{2c}^H < q^H < 0.94q_{2c}^H$) and that q^S decreases monotonically from $0.92q_{2c}^S$ at $R = 6280$ to $0.77q_{2c}^S$ at $R = 8920$. A four wave resonance condition also applies for the stripe superlattices. For the stripe superlattices the condition is given by

$$\pm 2\mathbf{q}_1^H = \pm(\mathbf{q}_1^S - \mathbf{q}_2^S). \tag{7}$$

This resonance condition is again a resonant tetrad between modes of two different wavenumbers and contains a harmonic 'self-interaction' term ($2\mathbf{q}_1^H$).

The noted prominence of the twelve modes satisfying resonant tetrad conditions (6) suggests the square superlattice patterns may be represented using the ansatz of a eigenmode expansion in the spirit of a weakly nonlinear analysis. The pattern field $T(\mathbf{x}, t)$, which is the shadowgraph intensity or mid plane temperature, may be defined as

$$T(\mathbf{x}, t) = \Re\{V^H(t) \sum_{j=1}^{2} A_j^H \exp(i\mathbf{q}_j^H \cdot \mathbf{x})\} +$$
$$\Re\{V^S(t) \sum_{j=1}^{4} A_j^S \exp(i\mathbf{q}_j^S \cdot \mathbf{x})\}, \tag{8}$$

where $\mathbf{x}$ is the horizontal coordinate parallel to the plane of the fluid layer. The time dependence of the harmonic and subharmonic eigenmodes [$V^H(t)$ & $V^S(t)$] is given by Floquet's theorem – $V^{H,S} = \Re\{\exp(\mu^{H,S}t) \sum_{n=0}^{\infty} c_n^{H,S} \exp(in\omega t)\}$,

normalized such that $|c_0^{H,S}| = 1$ – with Floquet exponents $\mu^H = 0$ for harmonic modes and $\mu^S = i\omega/2$ for subharmonic modes. Since the mode V^H is essentially sinusoidal about nonzero mean, only the first two terms ($n = 0$ & $n = 1$) need to be retained [25]. In contrast, V^S requires several higher harmonics of $\omega/2$. To represent the snapshot of a regular square superlattice [Fig. 17(b)], where the spectral peaks form rectangles, only two constant real amplitudes A and B with $A = A_1^H = -A_2^H$, $B = A_1^S = A_2^S = A_3^S = A_4^S$ are needed in (8). The amplitudes of the dominant Fourier modes in (8), which are directly available from the numerical temperature field, exhibit time dependence that is very well represented by $AV^H(t)$ and $BV^S(t)$ with adjusted amplitudes A, B [25]. The stripe superlattice pattern (Fig. 19) can be described analogously by (8) with one harmonic amplitude A^H and two subharmonic amplitudes $A_{1,2}^S$, where $A_1^S = A_2^S = iB$.

Inversion symmetry (both Boussinesq and subharmonic time-translation) plays an essential role in both the temporal dependence of the eigenmodes and the magnitudes of amplitudes in (8). The subharmonic eigenmodes (V^S), regardless of the presence of Boussinesq symmetry, are subject to the temporal inversion symmetry of time-translation. Higher harmonics of V^S must satisfy $V^S(t+\tau) = -V^S(t)$. In the non-Boussinesq experiments and numerics quadratic couplings between the harmonic modes are allowed. Resonant triads from quadratic interactions in the harmonic component are responsible for the harmonic hexagons observed in the vicinity of the bicritical point and for delaying the onset of square superlattices. In the Boussinesq numerics, inversion symmetry rules out quadratic couplings and requires those amplitudes to be zero. At cubic order the equation describing A_1^H has the common terms $\sim A_1^H|A_j^H|^2$ $(j = 1, 2)$ and $\sim A_1^H|A_j^S|^2$ $(j = 1 \ldots 4)$ existing with different coupling constants. However, according to (6) additional resonant coupling terms $\sim A_2^H A_1^S (A_2^S)^*, (A_2^H)^* A_3^S (A_4^S)^*$ play a crucial role. It should be noted that two phases for the four subharmonic amplitudes remain arbitrary within the amplitude equations up to cubic order. To fix them, higher order resonances, which are automatically included in (5), come into play. The analogous coupled amplitude equations for the stripe superlattice pattern contain a resonant coupling $\sim (A^H)^* A_1^S \, (A_2^S)^*$.

5.4 Other Frequencies

Differences in the dependence sensitivity of q^H and q^S on ω provide a means of changing superlattice structure. The ratio q^S/q^H is then a convenient parameter to change, where q^H depends weakly on ω and q^S depends strongly on ω. A limited number of simulations of (5) were performed to search for superlattices at other ω. Superlattices at $\omega = 40$ [Fig. 22(a)] are composed of a harmonic square sublattice and a subharmonic sublattice that is described by eight subharmonic peaks [Fig. 22(b)] qualitatively similar to the square superlattice power spectrum at $\omega = 98.0$. In this case, the wavenumber ratio is $q^S/q^H = 2.24$. At $\omega = 300$ numerics again find superlattices [Fig. 22(c)],

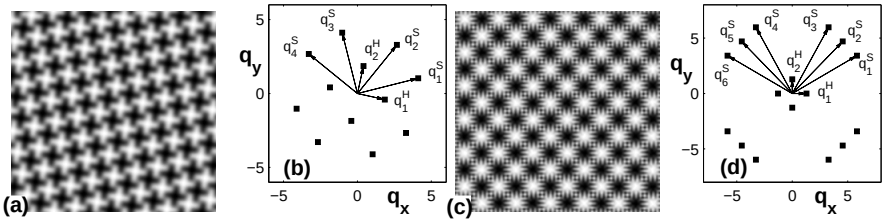

Fig. 22. Superlattices (*simulations*) and power spectrum at other ω values: (**a** & **b**) $\omega = 40$ and (**c** & **d**) $\omega = 300$.

this time with a much larger $q^S/q^H = 5.42$. Again, the harmonic sublattice displays regular square symmetry. However, the subharmonic sublattice is composed of stripes of two different orientations. In all cases studied, the superlattice patterns satisfied resonant tetrad conditions similar to (6).

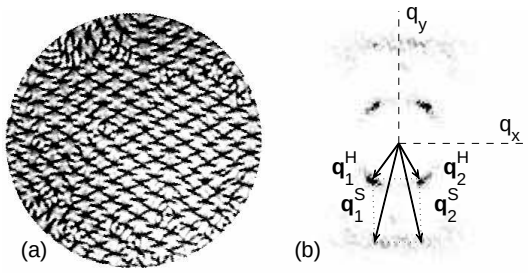

Fig. 23. Superlattice (*experiment*) at $\omega = 50.4$ (**a**) and its power spectra (**b**) at $Pr = 0.928$, $\delta Fr \approx 8.92 \times 10^{-4}$, & $R = 5180$.

Experiments were also performed to search for superlattices at other ω values. Figure 23(a) displays the superlattice found in experiments performed for $\omega = 50.4$. The harmonic sublattice is well-defined by two pairs of spectral peaks [Fig. 23(b)] while the subharmonic sublattice is also defined by two pairs of peaks, in contrast to the four pairs of peaks found for square superlattices at $\omega = 98$. These *rhombic superlattices* also satisfy resonant tetrad conditions [Fig. 23(b)].

6 Discussion

We have described initial results from studying pattern formation driven both thermally and by vertical oscillations. In the limits of weak and strong vertical oscillations the geometry-induced and dispersion-induced instabilities dominate pattern formation, respectively. Confirmations of linear sta-

bility predictions and pure state patterns are consistent with expectations. When the harmonic and subharmonic temporal responses are mutually stable we found a number of novel patterns, including superlattices. These exotic states were found numerically to emerge directly from conduction at a bicritical (codimension-two) point. A formation mechanism was proposed that is qualitatively different than the resonant triad interactions used to explain quasicrystals and superlattices recently reported in other pattern forming systems. The majority of this investigation was performed at $\omega \approx 100$. Glimpses of the patterns at other values of ω suggest there are many other interesting directions of investigation for acceleration-modulated Rayleigh-Bénard.

The work at the Georgia Institute of Technology is supported by NASA–Office of Life and Microgravity Sciences Grant NAG3-2006.

References

1. E. Bodenschatz, W. Pesch, G. Ahlers: Annu. Rev. Fluid Mech. **32**, 709 (2000)
2. M.C. Cross, P.C. Hohenberg: Rev. Mod. Phys. **65**, 851 (1993)
3. C. Bowman, A. C. Newell: Rev. Mod. Phys. **70**, 289 (1998)
4. M. Faraday: Philos. Trans. R. Soc. London **121**, 299 (1831)
5. M. Boucif, J.E. Wesfreid, E. Guyon: Eur. J. Mech. A. **10**, 641 (1991)
6. P. Coullet, T. Frisch, G. Sonnino: Phys. Rev. Lett. **49**, 2087 (1994)
7. C. Szwaj, S. Bielawski, D. Derozier, T. Erneux: Phys. Rev. Lett. **80**, 3968 (1998)
8. W. van Saarloos, J. D. Weeks: Phys. Rev. Lett. **74**, 290 (1995)
9. M. Silber, A.C. Skeldon, Phys. Rev. E **59**, 5446 (1999)
10. E. Bodenschatz, J.R. de Bruyn, G. Ahlers, D.S. Cannell: Phys. Rev. Lett. **67** 3078 (1991)
11. F. H. Busse, J. Fluid. Mech. **30**, 625 (1967)
12. W.S. Edwards, S. Fauve: Phys. Rev. E **47**, R788 (1993); J. Fluid Mech. **278**, 123 (1994)
13. A. Kudrolli, B. Pier, J.P. Gollub: Physica D **123**, 99 (1998)
14. C. Wagner, H.W. Müller, K. Knorr: Phys. Rev. Lett. **83**, 308 (1999)
15. L. M. Pismen, B. Y. Rubinstein: Chaos, Solitons and Fractals **10**, 761 (1999)
16. R. Lifshitz: Rev. Mod. Phys. **69**, 1181 (1997)
17. H. Arbell, J. Fineberg: Phys. Rev. Lett. **81**, 4384 (1998)
18. H. Arbell, J. Fineberg: Phys. Rev. Lett. **84**, 654 (2000)
19. H. Pi, S. Park, J. Lee, K.J. Lee: Phys. Rev. Lett. **84**, 5316 (2000)
20. E. Pampaloni, P.L. Ramazza,S. Residori, F.T. Arecchi: Phys. Rev. Lett. **74**, 258 (1995)
21. E. Pampaloni, S. Residori, S. Soria, F.T. Arecchi: Phys. Rev. Lett. **78**, 1042 (1997)
22. P. M. Gresho, R. L. Sani: J. Fluid Mech. **40**, 783 (1970)
23. R. Clever, G. Schubert, F.H. Busse: J. Fluid Mech. **253**, 663 (1993)
24. J.L. Rogers, M.F. Schatz, J.L. Bougie, J.B. Swift: Phys. Rev. Lett. **84**, 87 (2000)
25. J.L. Rogers, M.F. Schatz, O. Brausch, W. Pesch: Phys. Rev. Lett. **85**, 4281 (2000)
26. J.L. Rogers: Modulated Pattern Formation: Stabilization, Complex-Order, and Symmetry. PhD thesis, Georgia Institute of Technology, Atlanta (2001) (http://cns.physics.gatech.edu/~jeff)

27. O. Brausch: PhD thesis, Rayleigh Bénard Konvektion f"ur verschiedene isotrope und anisotrope Systeme, Physikalisches Institut der Universität Bayreuth, Bayreuth (2001)
28. V. Croquette: Contemp. Phys. **30**, 113 (1989); **30**, 113 (1989)
29. J.R. de Bruyn, E. Bodenschatz, S.W. Morris, S.P. Trainoff, Y. Hu, D.S. Cannell, G. Ahlers: Rev. Sci. Instrum. **67**, 2043 (1996)
30. W. Pesch: Chaos **6**, 348 (1996)
31. B. B. Plapp, D. A. Egolf, E. Bodenschatz, W. Pesch: Phys. Rev. Lett. **81** 5334 (1998)
32. S. W. Morris, E. Bodenschatz, D. S. Cannell, G. Ahlers: Physica D **97** 164 (1996)
33. C. W. Meyer, D. S. Cannell, G. Ahlers: Phys. Rev. A **45**, 8583 (1992)
34. V. Croquette: Contemp. Phys. **30**, 113 (1989); **30**, 153 (1989)
35. Y. Hu, R. Ecke, G. Ahlers: Phys. Rev. E **51** 3263 (1995)
36. M. C. Cross: Phys. Rev. A **25**, 1065 (1982)
37. U. E. Volmar, H. W. Müller: Phys. Rev. E **65**, 5432 (1997)